Materials Today Sustainability 28 (2024) 100950

Contents lists available at ScienceDirect

Materials Today Sustainability

journal homepage: www.journals.elsevier.com/materials-today-sustainability

# Hybridization of $CuFe_2O_4$ by carbon microspheres with improved charge storage characteristics for high energy density solid-state hybrid supercapacitor

J.J. Rushmittha [a,c], S. Radhika [b,c,**], Khalid A. Alrashidi [d], G. Maheshwaran [e], S. Dhinesh [f], S. Sambasivam [e,*]

[a] Department of Physics and Research Centre, Women's Christian College, Nagercoil, Tamilnadu, India
[b] Department of Physics, Pioneer Kumaraswamy College, Nagercoil, Tamil Nadu, India
[c] Manonmaniam Sundaranar University, Abishekapatti, 627012, Tirunelveli, Tamil Nadu, India
[d] Department of Chemistry, College of Science, King Saud University, Riyadh, 11451, Saudi Arabia
[e] National Water and Energy Center, United Arab Emirates University, Al Ain, 15551, United Arab Emirates
[f] Department of Physics, M.Kumarasamy College of Engineering (Autonomous), Thalavapalayam, Karur, 639 113, Tamilnadu, India

ARTICLE INFO

*Keywords:*
Energy storage
Hybrid nanocomposite
Copper ferrite
Solid-state supercapacitor
Carbon sphere

ABSTRACT

The hybrid nanocomposite of Copper Ferrite/Carbon sphere ($CuFe_2O_4$/C-sphere NC) has been synthesized and their combined electrochemical activity for supercapacitors is achieved. XRD study reveals the average crystallite size of $CuFe_2O_4$/C-sphere NC as 112 nm. $CuFe_2O_4$/C-sphere NC provides a huge specific surface area of 532 $m^2$/g. Cyclic voltammetry (CV) analysis exhibits the competitive specific capacity of $CuFe_2O_4$/C-sphere NC as 320 C/g at the sweep rate of 10 mV/s. The galvanostatic charge-discharge (GCD) study shows a good specific capacity of 264 C/g at 1 A/g and excellent cyclic stability of 82.4% for 5000 cycles. The $CuFe_2O_4$/C-sphere//AC solid-state hybrid supercapacitor provides a high specific capacity of 131 C/g along with remarkable energy density and power density of 40.9 Wh/kg and 11248 W/kg respectively.

## 1. Introduction

In the present world of advanced technologies and ultrafast communications, the requirement for sustainable, quick-responding, and long-lasting energy devices is extensively attaining scale and momentum. The existing technologies powered with lithium-ion batteries fail to resolve the high power requirements. To overcome these issues, researchers are intensively focused on developing energy storage devices that hold both higher energy density and high power density [1,2]. Supercapacitors offer outstanding power densities, remarkable cyclic stability, ultrafast charge-discharge rates, and are more environmentally friendly than lithium-ion batteries and conventional capacitors, but they deliver unsatisfactory energy density [3]. To further improve the energy density and high charge accumulating capability, the enhancement of the specific capacity of the electrodes as well as widening the operating window of the device should be achieved. Here, the improved specific capacitance can be achieved by tuning the electrode geometrical architecture, improving the surface area, forming of mesoporous structure, developing of heterostructure, and maintaining the wettability [4]. Further, the wide potential window can be achieved by choosing the appropriate electrolytes for the fabrication of devices with specified configurations such as symmetric, asymmetric, and hybrid devices. The main challenge is to select the electrode with perfect geometry that offers high electrical conductivity, large surface area, and multiple oxidation states that support efficient charge transport, and hybrid structures that enable the use of different charge storage processes to improve the charge accumulation and storage [5–8].

Electrode materials are categorized based on their mode of storing the charges, subsequently, the electric double layer capacitors (EDLCs), pseudocapacitors (PCs), and hybrid capacitors (HCs). In EDLCs, the surface adsorption process occurs at the outer surface of the electrode/electrolyte interfacial region which utilizes the mesoporous carbons as electrodes, whereas in pseudocapacitors, the reversible rapid surface redox process takes place which results in the intercalation of ions into

* Corresponding author, National Water and Energy Center, United Arab Emirates University, Al Ain 15551, UnitedArab Emirates
** Corresponding author, Department of Physics, Pioneer Kumaraswamy College, Nagercoil, Tamil Nadu, India
*E-mail addresses:* radhisatha@yahoo.com (S. Radhika), s_sambasivam@uaeu.ac.ae (S. Sambasivam).

https://doi.org/10.1016/j.mtsust.2024.100950
Received 11 June 2024; Received in revised form 19 July 2024; Accepted 3 August 2024
Available online 3 August 2024

the nearer atomic surface layers where the metal oxides, hydroxides, sulfides, and polymers as the supercapacitor electrodes [9,10]. Recently, diverse transition metal oxides were utilized as electrodes for supercapacitors due to their unique quantum chemistry, generation of abundant electrochemically active sites, and high conductivity [11,12]. Among the binary transition metal oxides, $NiCo_2O_4$ is known to be the standard and most potential material for supercapacitor applications. In this way, numerous binary transition metal oxides like $CuCo_2O_4$ [13], $ZnCo_2O_4$ [14], $MgCo_2O_4$ [15], $MnCo_2O_4$ [16], etc have been recently synthesized and successfully applied as the electrode materials for supercapacitors. This binary cobalt series with its unique morphologies exhibits good specific capacity and energy density values, but, they also hold their limitations such as stability, conductivity, surface area, and internal resistance values which varies one another [17,18]. Among all other binary cobalt oxides, $CuCo_2O_4$ microtubes deliver a high specific capacity value of about 393.66 C/g at the current density of 1 A/g with a high energy density of about 32.49 W h/kg [13].

Currently, the binary magnetic ferrites like $NiFe_2O_4$, $ZnFe_2O_4$, $CuFe_2O_4$, etc are broadly utilized as supercapacitor electrodes due to their advantage of multiple metal cations that results in improving electrochemical activity [19]. More specifically, $CuFe_2O_4$ holds benchmark characteristics as an excellent material for supercapacitors than any other ferrites due to their distinctive electronic configuration like $3d_{10}$ $4s_1$ and excellent physicochemical properties that result in offering extraordinary specific capacitance, longer cycle life, and competitive energy density [20]. However, it suffered from low rate capability, slow reaction kinetics, and morphological collapse owing to the successive charge-discharge process [21,22]. To address these problems, the construction of composites by introducing carbonized materials with metal oxides is an effective way to tune the electronic structure, increase the conductivity, facilitate the volume extension while the repeated charge/discharge process occurs, and enhance the rate capability [23,24]. Specifically, Carbon spheres are the potential capacitive electrode material with a large active surface area, mesoporous nature, good mechanical stability, and lower specific density which facilitates the transfer of ions, and enhances the electrochemical activity by shortening the diffusion pathways of the electrolytic ions in the electrode structure. Apart from these characteristics, carbon spheres promote the expansion and contraction of volume during the charging and discharging process resulting in improved structural stability with a long cycle life [25,26].

There are numerous literature that reports the electrochemical activity of the $CuFe_2O_4$ composite with carbonaceous materials for supercapacitors. For example, Israr et al. [27] synthesized that the $CuFe_2O_4$ and graphene nanoplatelet nanocomposites ($(CuF)_{1-x}(GNPs)_x$) by an in-situ co-precipitation method. The as-prepared $(CuF)_{1-x}(GNPs)_x$ demonstrated the high specific capacitance of about 264 F/g at the current density of 0.5 A/g and also it delivers good cyclic stability of 74% for 1000 cycles. The symmetric supercapacitors were assembled, providing the energy and power densities of 8.6 W h/kg and 125 W/kg respectively. Similarly, Ghasemi et al. [27], reported that the PANI/GO/$CuFe_2O_4$ ternary hybrid nanocomposite as electrode material for supercapacitors. The fabricated ternary PANI/GO/$CuFe_2O_4$ electrode demonstrated a high specific capacitance of 614.76 F/g at a current density of 1 A/g along with the cyclic stability of about 88% for 3500 cycles. The asymmetric supercapacitor based on PANI/GO/$CuFe_2O_4$//GO was fabricated, delivering the specific capacitance of 124 F/g at 1 A/g and also the energy and power densities of 49.72 W h/kg and 923 W/kg respectively. Further, Whon-hee Lee et al. [28], synthesized the nitrogen-doped carbon spheres by emulsifying the polymerized polystyrene-based colloidal spheres with melamine 1,3,5-triazine-2,4,6-triamine (nitrogen-rich molecule) by pyrolytic carbonization method. The nitrogen-doped carbon spheres demonstrated an excellent specific capacitance of 191.9 F/g at 0.1 A/g and a capacitance retention of 110% even after 10000 charge-discharge cycles.

In the present work, we have synthesized the binary $CuFe_2O_4$ nanoparticles by a simple and cost-effective co-precipitation technique. The $CuFe_2O_4$ nanoparticles store the charges through the faradaic redox reactions by the insertion/desertion of ions in their electrode structure which results in delivering the high specific capacity with improved energy density. Though the faradaic reaction is sluggish, it requires more time to charge the electrode than the typical supercapacitors and also it can accommodate only the limited ions due to their limited redox active sites [29,30]. To improve the specific capacity and to generate more active sites for the electrochemical reactions, the EDLC-type carbon spheres are incorporated into the $CuFe_2O_4$ nanoparticles which can deliver the numerous redox active sites, large surface area, high electrical conductivity, rapid charge-discharge characteristics, low internal impedance, and good electrode stability. The fabricated Copper Ferrite/Carbon sphere ($CuFe_2O_4$/C-sphere NC) demonstrates a high specific capacity of 264 C/g at 1 A/g and can withstand 5000 cycles with a capacitive retention of 82.4%. Moreover, the achievement of high energy density is the major goal of this research, which can be fulfilled by fabricating a solid-state hybrid supercapacitor that delivers a widened operating potential with excellent energy and power densities. The solid-state hybrid supercapacitor made of $CuFe_2O_4$/C-sphere as cathode and AC as anode was fabricated which delivers the high specific capacity of 131 C/g together with the energy and power densities of 40.9 W h/kg and 11248 W/kg respectively.

## 2. Experimental procedure

### 2.1. Synthesis of $CuFe_2O_4$ nanoparticles

In a typical synthesis technique, 1 M of $CuCl_2$ and 2 M of $FeCl_3$ were slowly dissolved in 30 mL of DI water at constant stirring and the precipitating reagent of 8 M of NaOH was mixed with the above processed solution. The entire reaction was processed at 80 °C and the pH = 12. Then, the precipitated solution was washed thrice with DI water and ethanol and heated at 900 °C for 5 h to synthesize $CuFe_2O_4$.

### 2.2. Synthesis of carbon spheres

Concisely, 1 M of glucose was dissolved in 80 mL of the DI water at constant stirring and hydrothermally heated at 180 °C for 12 h. Then, the resultant solution was washed several times with DI water subsequently with ethanol and finally, vacuum dried at 80 °C for 12 h to get Carbon spheres.

### 2.3. Synthesis of $CuFe_2O_4$/Carbon sphere nanocomposite

$CuFe_2O_4$/Carbon sphere nanocomposite was prepared by sonicating 0.2 g of $CuFe_2O_4$ and 0.02 g of Carbon sphere in 30 mL of DI water and centrifuged at 3000 RPM. Finally, the resulting sample was vacuum dried at 80 °C for 12 h to get $CuFe_2O_4$/Carbon sphere nanocomposite. The complete synthesis method is presented in Fig. 1.

### 2.4. Electrode fabrication technique and electrochemical characterization

The working electrode featured a Nickel foam current collector, which underwent a thorough cleaning process involving 1 M HCl, ethanol, and DI water to prevent any additional contamination. The slurry for the electrode was prepared by grinding 80% active material, 10% PVDF binder, and 10% activated carbon in N-methyl-2-Pyrrolidone (NMP). The resulting homogeneous slurry was then applied to 1 × 1 $cm^2$ Ni foam dimensions and subjected to vacuum drying at 80 °C for 12 h.

To study the electrochemical characteristics of the fabricated electrodes, the Squidstat potentiostat instrument was utilized, employing a platinum rod as the working electrode, and KCl saturated Ag/AgCl as both the counter and reference electrodes. The specific capacitance of the carbon sphere electrode material was evaluated from CV and GCD as

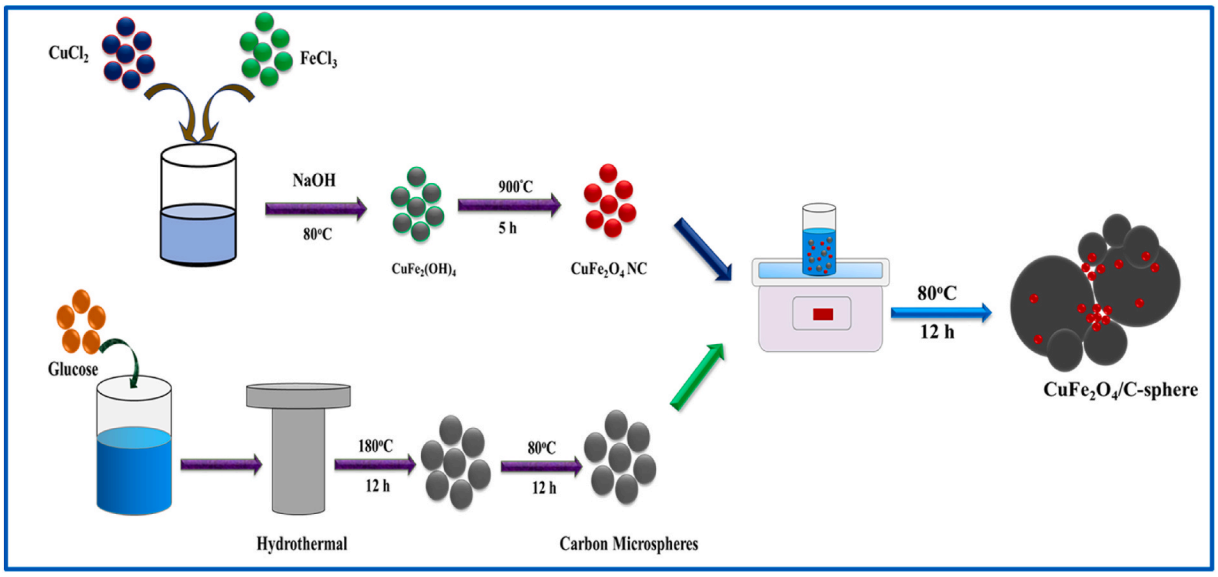


**Fig. 1.** Synthesis scheme of $CuFe_2O_4$/c-sphere NC.

$$C_{sp1} = \frac{\int I(V)dV}{\Delta V\, m_1 v} \quad (1)$$

$$C_{sp2} = \frac{I\Delta t}{m_1 \Delta v} \quad (2)$$

The specific capacity of battery-type electrodes was evaluated by

$$C_{sp3} = \frac{\int I(v)\, dV}{(m_1)(v)} \quad (3)$$

$$C_{-}(sp4) = \frac{I\Delta t}{(m_1)} \quad (4)$$

where $C_{sp1}$ and $C_{sp2}$ are the specific capacitance from CV and GCD analyses respectively and $C_{sp3}$ and $C_{sp4}$ are the specific capacity of CV and GCD analyses respectively, I(V) is the current, $m_1$ - mass of the coated active material, v - scan rate (mV/s), and $\Delta t$ is the discharge time.

### 2.5. Synthesis of PVA-KOH gel polymer electrolyte

Briefly, 0.5 g of polyvinyl alcohol was added to 30 mL of DI water and heated at 90 °C until it was fully dissolved. Then, 0.5 g of KOH was added to the above solution and stirred at 90 °C for 3 h until it got yellowish gel. The resultant gel was then coated on the surface of the anode and cathode and allowed to solidify.

### 2.6. Fabrication of $CuFe_2O_4$/C-sphere//AC solid state hybrid supercapacitor

Solid state hybrid supercapacitor (SHC) device was assembled by using the cathode as $CuFe_2O_4$/C-sphere NC and the anode of AC in between these electrodes, the Whatman filter paper was used as the separator, and PVA-KOH as the gel electrolytic medium. The specific capacity $C_{sp\ SHC}$ of the SHC device was estimated from the formula

$$Csp_{SHC} = \left(\frac{I\Delta t}{m_2}\right) \quad (5)$$

The Energy density ($E_{SHC}$), as well as the power density ($P_{SHC}$) of the $CuFe_2O_4$/C-sphere//AC SHC device, were evaluated from the formula

$$E_{SHC} = \frac{1}{7.2}\, C_{sp\ SHC}\, (\Delta V)^2 \quad (6)$$

$$P_{SHC} = 3600 * \frac{E}{\Delta t} \quad (7)$$

where $Csp_{SHC}$ was the specific capacity calculated from the discharge curves of the GCD profile and $m_2$ is the total mass (g) which is the sum of the mass of the cathode and anode.

## 3. Characterization techniques

The X-ray diffractometer (PANalytical X'Pert PRO) was utilized to examine the structural parameters of the $CuFe_2O_4$/C-sphere, utilizing a Cu Kα X-ray source. The surface morphology, surface nature, and elemental distribution were visualized using a Field Emission Scanning Electron Microscope (CARL ZEISS EVO 18) equipped with an EDAX spectrometer (Quantax 200 with X-Flash – Bruker). High-Resolution Transmission Electron Microscope (HR-TEM JOEL-2100+) was utilized to analyze particle size, surface morphology, and d-spacing of $CuFe_2O_4$/C-sphere. Additionally, the BET instrument (BELSORP-maxII) was employed to evaluate surface area and pore size distribution.

## 4. Results and discussion

### 4.1. X-ray diffraction

XRD pattern was analyzed using an XPert Pro X-ray diffractometer. XRD pattern shows the formation of pure $CuFe_2O_4$ with good crystallinity and their corresponding peaks were 2θ = 18.3, 29.9°, 30.5, 34.7°, 35.8°, 37.1°, 57.8°, 62.1°, and 63.6° corresponds to their planes (101), (112), (200), (103), (211), (422), (321), (224), and (400) which was confirmed by JCPDS card: 34–0425 [31,32]. Similarly, the XRD pattern of the C-sphere displays two broad peaks at 23° and 43°, corresponding to the (002) and (100) planes, respectively. Notably, the XRD pattern of $CuFe_2O_4$/C-sphere NC (Fig. 2) exhibits no significant peak shifts, but, there is a slight increase in the amorphous nature, confirming the incorporation of C-sphere into the $CuFe_2O_4$ lattice.

The determination of crystallite sizes employed the Debye-Scherrer formula:

$$D = 0.9\lambda/\beta Cos\theta \quad (8)$$

Here, D represents the crystallite size, λ is the X-ray radiation wavelength, β is the full-width half maximum, and θ is the diffraction angle. The calculated average crystallite size for $CuFe_2O_4$/C-sphere NC

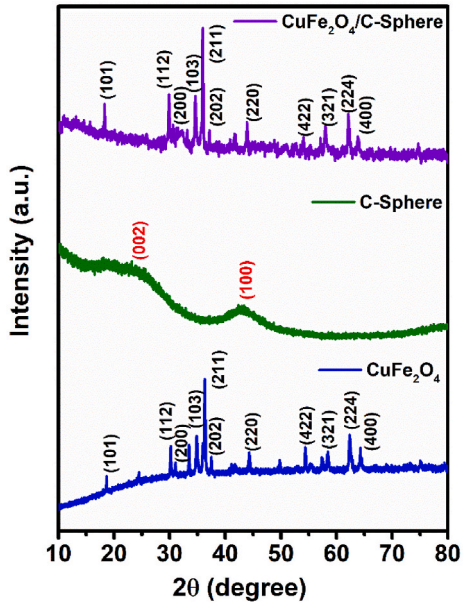


**Fig. 2.** XRD pattern of $CuFe_2O_4$, C-sphere, and $CuFe_2O_4$/C-sphere NC.

was found to be 112 nm.

### 4.2. BET analysis

$N_2$ adsorption-desorption isotherms were investigated using Brunauer-Emmett-Teller (BET) study. The $N_2$ sorption study reveals a similar H3-type hysteresis curve for all samples, representing type-II isotherms [33]. In addition, the active surface area of $CuFe_2O_4$, C-sphere, and $CuFe_2O_4$/C-sphere NC was 78, 512, and 532 $m^2/g$ correspondingly (Fig. 3a), signifying the substantial increase of the surface of $CuFe_2O_4$ by the incorporation of C-sphere. Similarly, the pore size of $CuFe_2O_4$, C-sphere, and $CuFe_2O_4$/C-sphere NC was 1.35 nm, 2.82 nm, and 2.65 nm respectively as presented in Fig. 3b. The obtained high surface area and mesoporosity of $CuFe_2O_4$/C-sphere NC effectively improves the electrochemical activity by minimizing both ion transport pathways and exposure of more surface active sites to involve in redox reactions [34].

### 4.3. SEM and EDX analysis

The surface morphology and particle size were studied by FESEM analysis. FESEM images show the existence of cubic-shaped $CuFe_2O_4$ with smooth-surfaced nanoparticles and the size of the particle was about 110 nm as depicted in Fig. 4a. Similarly, the surface morphology of C-spheres reveals the presence of well-aggregated microspheres with smooth surfaced morphology, and the average sphere size of 750 nm (Fig. 4b). Notably, the morphology of $CuFe_2O_4$/C-sphere NC reveals the co-existence of both the cubic shaped $CuFe_2O_4$ nanoparticles and carbon microspheres with the average particle size of 723 nm (Fig. 4c) [35].

The elemental distribution, chemical composition, and purity were confirmed by EDX Spectroscopy analysis. EDX mapping confirms (Fig. 4d-h) the evenly distributed particles with high purity and their corresponding weight ratios of 41 wt% of C, 18 wt% of Fe, 34 wt% of O, and 7 wt% of Cu. In EDX mapping, there is no other elemental traces were observed, revealing the high-purity nature of the $CuFe_2O_4$/-C-sphere NC [36].

### 4.4. HRTEM analysis

HR-TEM reveals the formation of smooth-surfaced cubic particles along with a well-aggregated smooth-surfaced microsphere with the size of the particle of 710 nm (Fig. 5a and b). Notably, there are some small particles were also observed at the C-sphere surface as represented in Fig. 5c. SAED analysis confirms the polycrystallinity of $CuFe_2O_4$/C-sphere NC (Fig. 5d), and their concentric rings were allotted to the lattice planes (211), and (101) which coincides with their XRD results [37].

### 4.5. XPS analysis

The oxidation states and composition of the $CuFe_2O_4$/C-sphere NC were analyzed using X-ray Photoelectron Spectroscopy (XPS). The survey spectrum revealed various oxidation states of copper, iron, oxygen, and carbon along with their respective binding energies, as depicted in Fig. 6a. The high-resolution XPS spectrum for Cu shows the presence of the Cu 2p doublet peaks Cu $2p_{1/2}$ and Cu $2p_{3/2}$ at binding energies of 944.5 eV and 933.2 eV, respectively as shown in Fig. 6b. Similarly, the high-resolution XPS spectrum for Fe indicates the Fe 2p doublet, with Fe $2p_{1/2}$ and Fe $2p_{3/2}$ peaks around 725.3 eV and 710.7 eV, correspondingly [38]. The deconvoluted Fe spectrum also shows the presence of $Fe^{3+}$ at a binding energy of 712.3 eV, as shown in Fig. 6c. Additionally, the deconvoluted O spectrum reveals a peak around 531.8 eV, which can be split into two peaks indicating the presence of $OH^-$ and O1s at binding energies of 533 eV and 531 eV, respectively as presented in Fig. 6d. The XPS spectrum for carbon shows peaks at 287 eV and 284.7 eV, corresponding to the chemical states of –C-O and –C═C-, respectively, as depicted in Fig. 6e [39].

### 4.6. Electrochemical studies

The electrochemical characteristics were studied in a three-electrode system in a 3 M KOH electrolyte medium. Moreover, the electrochemical properties of $CuFe_2O_4$ and C-sphere were studied separately. CV curves of $CuFe_2O_4$ were measured within 0–0.6 V, revealing the typical battery-

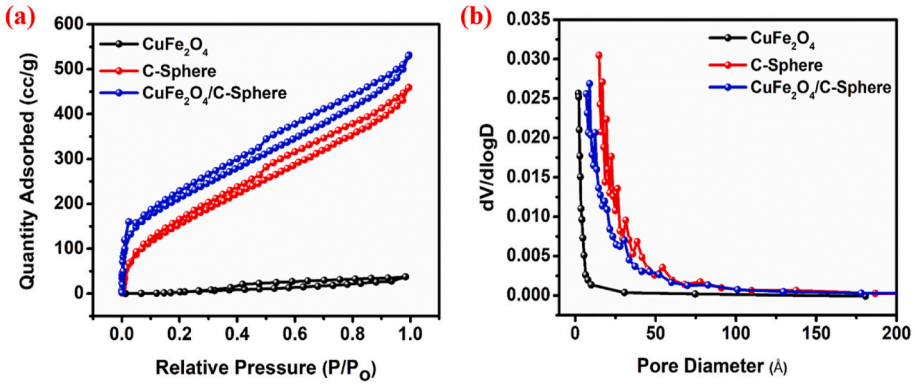


**Fig. 3.** BET analysis (a) $N_2$ sorption study (b) pore size distribution of $CuFe_2O_4$, C-sphere, and $CuFe_2O_4$/C-sphere NC.

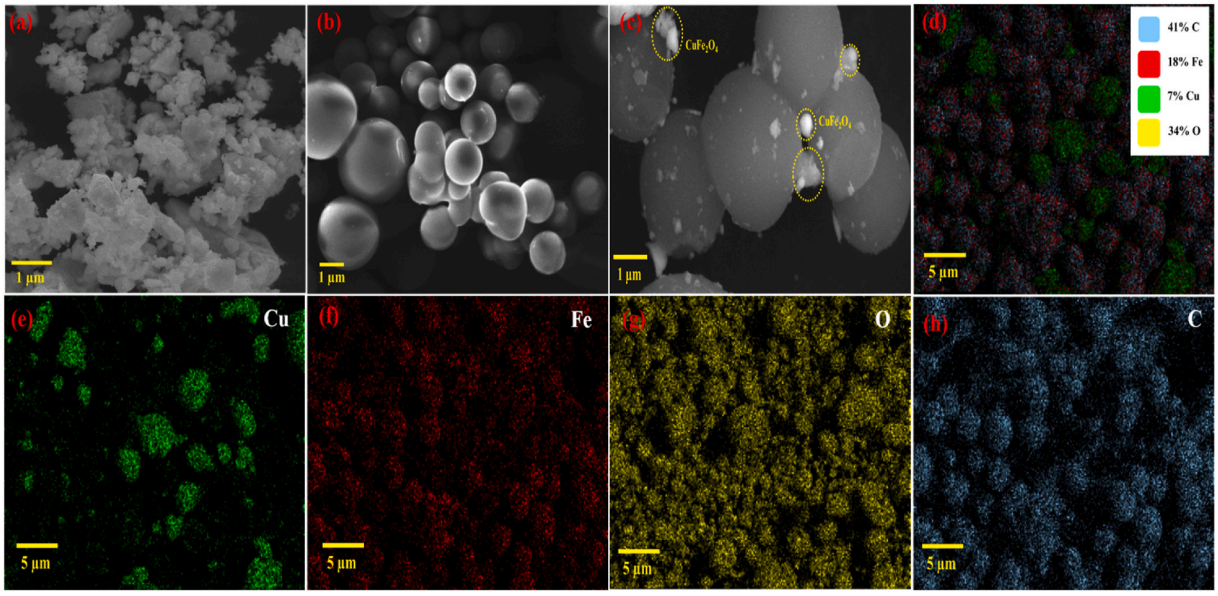


**Fig. 4.** SEM images of (a) $CuFe_2O_4$, (b) C-sphere, and (c) $CuFe_2O_4$/C-sphere NC, (d–h) EDX mapping of $CuFe_2O_4$/C-sphere NC.

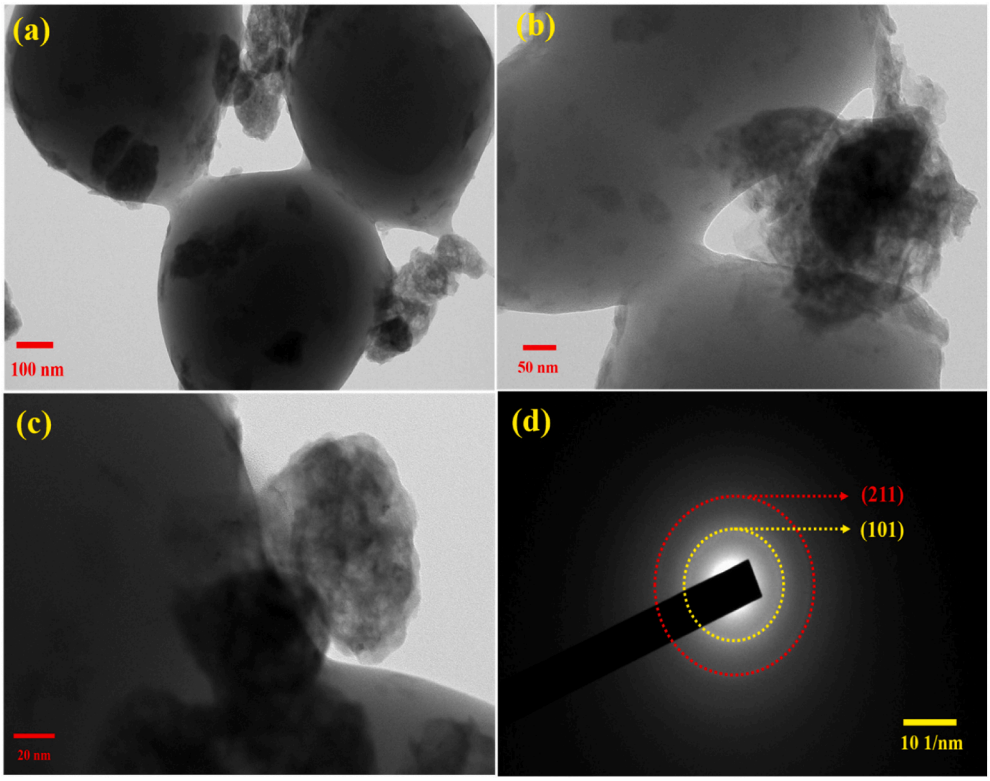


**Fig. 5.** (a–c) HETEM image and (d) SAED pattern of $CuFe_2O_4$/C-sphere NC.

like behavior with good reversibility and high rate capability and their calculated specific capacities are 200.5, 164, 119, 93.6, and 78C/g correspond to scan rates 10–200 mV/s correspondingly as shown in Fig. S1a. Likewise, the CV profile of the C-sphere (Fig. S2a) was analyzed within −1 V–0 V which demonstrates typical EDLC behavior and their obtained specific capacitances are 402, 388, 353, 302, and 274 F/g corresponds to sweep rates 10–200 mV/s respectively.

Remarkably, CV curves of $CuFe_2O_4$/C-sphere NC (Fig. 7a) show typical battery-like characteristics that provide excellent reversible CV curves along with a large integral area, signifying their enhanced electrochemical activity owing to their combined charge storage process as well as the synergistic effect of $CuFe_2O_4$ and C-sphere NC, generation of multiple cations, and improved surface area [40,41]. The calculated specific capacities are 320, 280, 250, 185, and 107.5C/g corresponding to sweep rates 10–200 mV/s.

The redox mechanism of $CuFe_2O_4$/C-sphere NC is shown in the equation as

$$CuFeO + OH^- \leftrightarrow CuFeO\,(OH) + e^- \quad (9)$$

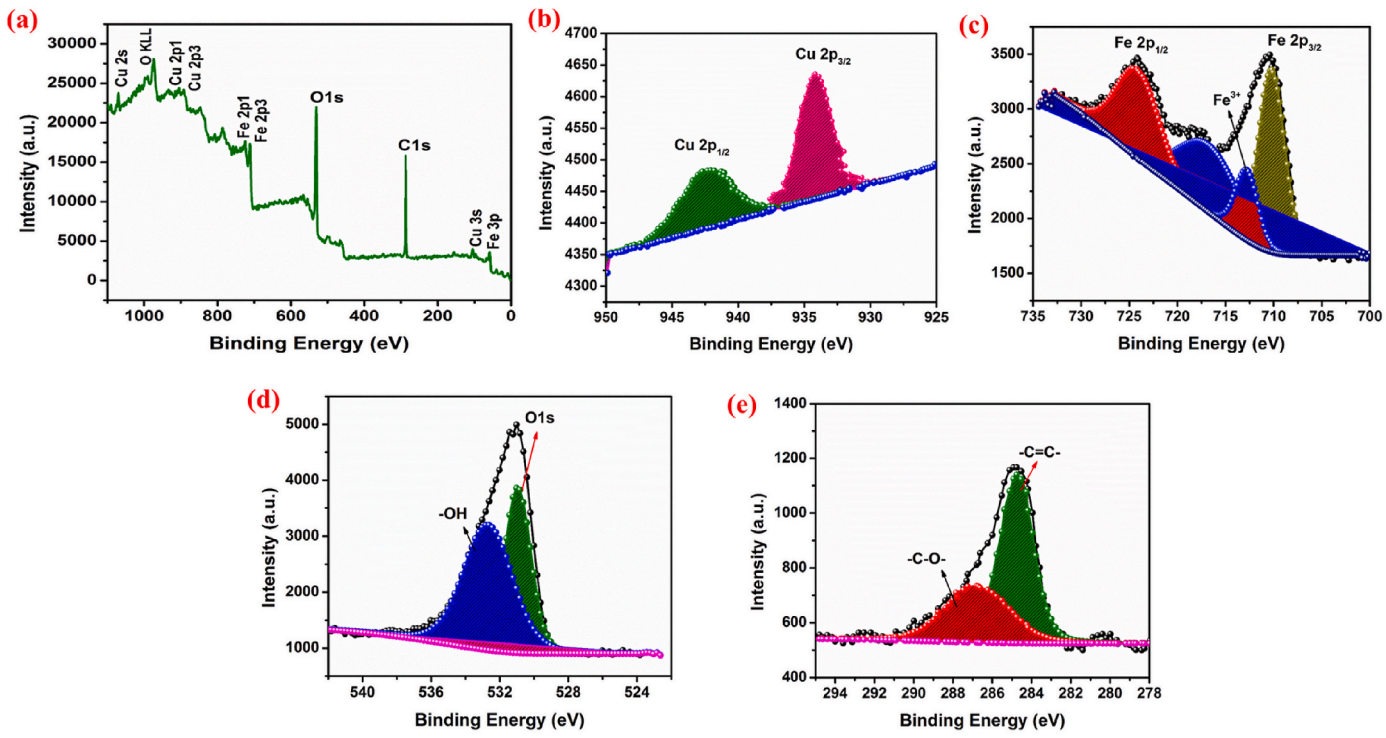


**Fig. 6.** XPS spectrum (a) Survey spectrum and Core level spectra of (b) Cu 2p, (c) Fe 2p, (d) O 1s, and (e) C 1s of $CuFe_2O_4$/C-sphere NC.

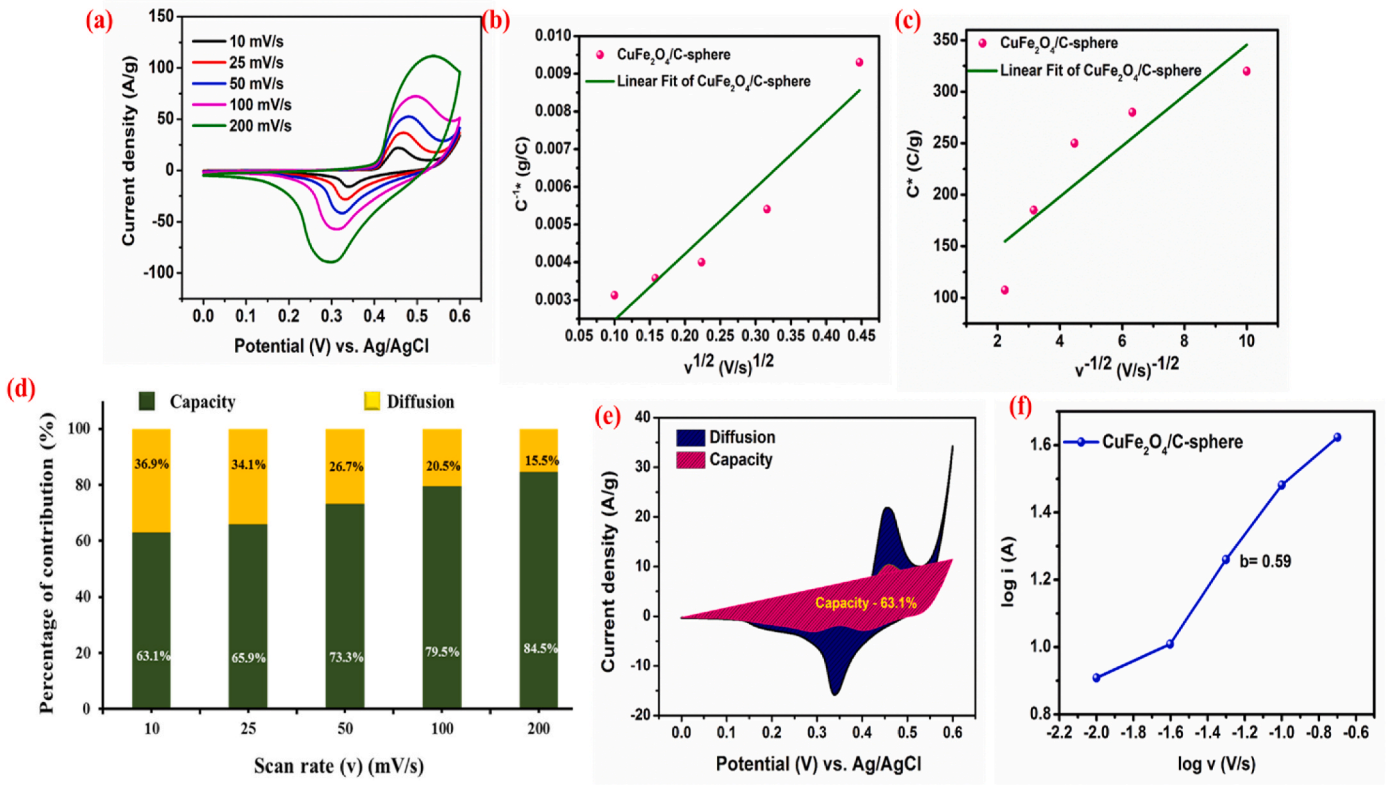


**Fig. 7.** (a) CV curves at different scan rates of 10–200 mV/s, (b) total capacity, (c) outer capacity, (d) Capacity-diffusion plot at different scan rates (10–200 mV/s), (e) Dunn plot at the scan rate of 10 mV/s, and (f) Calculation of b value of $CuFe_2O_4$/C-sphere NC.

$$CuO + OH^- \leftrightarrow CuO(OH) + e^- \quad (10)$$

$$FeO + OH^- \leftrightarrow FeO(OH) + e^- \quad (11)$$

More information regarding the charge storage process was studied through the Trasatti method. From the Trasatti method, it is possible to differentiate the capacitive and diffusion currents from the CV curve and the net charge accumulated at the electrode is the sum of capacitive

contribution and diffusion contributions as

$$C*_{total} = C*_{inner} + C*_{outer} \quad (12)$$

Also, Trasatti differentiated the surface-controlled reactions and intercalation-de-intercalation as a function of scan rate as

$$i(V) = k_1\, v + k_2\, v^{1/2} \quad (13)$$

$$\frac{i(V)}{v^{1/2}} = k_1\, v^{1/2} + k_2 \quad (14)$$

here, $k_1$ and $k_2$ are the capacity contribution factor and diffusion-controlled contribution factor.

Besides, the total charge accumulated internally ($C^*_{Total}$) and the charge adsorbed at the electrode surface ($C^*_{outer}$) can be separated as [42]

$$C^*(V) = k * \frac{1}{v^{1/2}} + C^*_{outer} \quad (15)$$

$$\frac{1}{C^*(V)} = k * v^{1/2} + \frac{1}{C^*_{Total}} \quad (16)$$

From equations (15) and (16), the total capacity ($C^*_{Total}$) can be estimated by linear fitting of $C^{-1}*$ vs $v^{1/2}$ at $v = 0$, and from the intercept of the linear fit, the total capacity of $CuFe_2O_4$ and $CuFe_2O_4$/C-sphere NC was calculated to be 358.4 and 833.4C/g, and for C-sphere, the total capacitance was 555 F/g as depicted in Fig.S1b, Fig.S2b, and Fig. 7b. Similarly, the outer capacity ($C^*_{outer}$) can be estimated from the intercept of the linear fit between $C^*$ vs $v^{-1/2}$ at $v = \infty$, and the obtained outer capacities were 69 and 106.3 C/g for $CuFe_2O_4$ and $CuFe_2O_4$/C-sphere NC correspondingly as portrayed in Fig.S1c and Fig. 7c. Moreover, the outer capacitance of the C-sphere was 46.4 F/g as presented in Fig. S2c.

Finally, the accumulation of the charges at the electrode structure can be evaluated by subtracting the outer capacity from the total capacity, and the resultant inner capacity ($C^*_{inner}$) was 289.4 and 727.03 C/g respectively for $CuFe_2O_4$ and $CuFe_2O_4$/C-sphere NC g and for C-sphere, the inner capacitance was 508.6 F/g.

Moreover, the capacitive-controlled and diffusion-controlled contributions were estimated from the equation as,

$$C*_{inner}\ (\%) = \frac{C*_{inner}}{C*_{Total}} \text{ x } 100\ \% \quad (17)$$

$$C*_{outer}\ (\%) = \frac{C*_{outer}}{C*_{Total}} \text{ x } 100\ \% \quad (18)$$

From equations (17) and (18), the percentage of diffusion contributions ($C*_{inner}$ (%)) calculated at the scan rate of 10 mV/s was 87.9%, 9.2%, and 36.9% and the percentage of capacitive controlled contributions ($C*_{outer}$ (%)) were evaluated as 12.1%, 90.8%, and 63.1% respectively for $CuFe_2O_4$, C-sphere, and $CuFe_2O_4$/C-sphere NC as shown in Fig.S1d, Fig.S2d, and Fig. 7d. It is observed from the Dunn plot, the capacity contribution of $CuFe_2O_4$/C-sphere NC (63.1%) greatly improved compared with the pure $CuFe_2O_4$ (12.1%), which is due to the presence of C-sphere (90.8%) that induces the surface controlled reaction in $CuFe_2O_4$/C-sphere NC as depicted in Fig.S1e, Fig.S2e, and Fig. 7e.

Furthermore, the above-discussed capacity enhancement can be confirmed by the power law,

$$I = av^b \quad (19)$$

where, v is the sweep rate (V/s), a and b are constants. The value of 'b' can be obtained by linear fitting the plot log (i) vs log v and taking the slope to get the b-value. As a result, the obtained b-value can be either 0.5 or 1. If the b-value is nearly 0.5, represents the battery-like charge storage mechanism, and if the b-value is nearly 1, indicating the capacitance or surface-controlled charge storage mechanism [43]. From the obtained b-values, the $CuFe_2O_4$ (Fig. S1f) shows purely battery-like behavior with the value of b = 0.45 and for C-sphere (Fig. S2f), the b-value is 0.69, indicating the capacitive type behavior. Finally, the $CuFe_2O_4$/C-sphere NC (Fig. 7f) delivers the b-value of 0.59, indicating the improvement in the surface-controlled reactions owing to the incorporation of the C-sphere in the $CuFe_2O_4$ lattice.

EIS analysis reveals the internal impedance of $CuFe_2O_4$/C-sphere NC measured within the frequency range 100 kHz–0.1 Hz [44]. The Nyquist plot shows the solution resistance ($R_s$) and charge transfer resistance ($R_{ct}$) of $CuFe_2O_4$ as 3.2 Ω and 5.04 Ω correspondingly and for.

C-sphere, $R_s$ and $R_{ct}$ were 2.13 Ω and 4.27 Ω respectively as shown in Fig. 8a. Noteworthy, $CuFe_2O_4$/C-sphere NC delivers the lower internal impedances compared to the individual electrodes which shows their improved electrical conductivity and their corresponding $R_s$ and $R_{ct}$ was 1.87 Ω and 2.8 Ω.

The charge-discharge characteristics were studied by GCD profiles. GCD curves of $CuFe_2O_4$ (Fig. 8b) show the asymmetric non-linear charge/discharge profiles which represent their battery-type behavior as discussed in CV studies and their competitive specific capacity was 138 C/g at 1 A/g. Similarly, the GCD curves of the C-sphere (Fig. 8c) deliver the symmetric charge-discharge profile which represents typical EDLC nature and their high specific capacitance was 322 F/g at 1 A/g [45]. Noteworthy, the discharge profile of $CuFe_2O_4$/C-sphere NC (Fig. 8d) delivers excellent electrochemical activity which is owing to the synergy effect of $CuFe_2O_4$ and C-sphere and also due to the generation of multiple redox active sites and the obtained specific capacity of 264 C/g at constant current of 1 A/g. The cyclic stability of $CuFe_2O_4$/C-sphere NC (Fig. 8e) was tested to evaluate the cycling performance for longer charge/discharge cycles and demonstrated stable capacitive retention of 82.4% for 5000 cycles.

### 4.7. Post-cyclic SEM analysis

The SEM analysis of the $CuFe_2O_4$/C-sphere NC after 5000 cycles represents the morphological variation after the continuous charging and discharging process. The long-term interaction between the electrolyte-electrode interfacial junctions degrades the surface of the active material and as a result the specific capacity and stability substantially decrease [46]. Herein, the SEM image of $CuFe_2O_4$/C-sphere NC after 5000 cycles maintains a morphology similar to their morphology before the cyclic stability test was conducted. In some cases, the morphology of the C-sphere (marked as yellow color in Fig. 9a) shows some deep pits which may be the starting stage of morphological degradation. From Fig. 9b, the SEM image reveals the agglomeration of $CuFe_2O_4$ nanoparticles present in $CuFe_2O_4$/C-sphere NC. From the SEM analysis, it is observed that the morphology of $CuFe_2O_4$/C-sphere NC after 5000 cycles remains the same with minor defects which confirms the stable structure of the electrode material.

### 4.8. Solid-state hybrid supercapacitor

Based on the electrochemical activity of the $CuFe_2O_4$/C-sphere NC, it is further scaled up to a solid-state hybrid supercapacitor (SHC). Prior to the device fabrication process, the charge of the anode and cathode should be balanced by using the mass balance equation, $\frac{m_+}{m_-} = \frac{C_- \Delta V_-}{C_+ \Delta V_+}$. Similar to the three-electrode configuration of $CuFe_2O_4$/C-sphere NC, the electrochemical characteristics of the anode (AC) were tested within the potential window of −1 to 0 V and the detailed electrochemical study was included in the supplementary information file (Fig. S3). From the electrochemical test of the anode, the calculated mass balance ratio was achieved to be 1:1.2 (as shown in Fig. 10a). SHC device was fabricated by assembling the AC anode, $CuFe_2O_4$/C-sphere cathode, and separator along with the PVA-KOH as the gel polymer electrolyte [47]. The cyclic voltammetry of the SHC provides the combined profile of AC and $CuFe_2O_4$/C-sphere NC within the wide operating voltage of 0–1.5 V and also it demonstrates the typical faradaic curves with specific redox peaks were observed. Also, the CV of $CuFe_2O_4$/C-sphere//AC SHC shows

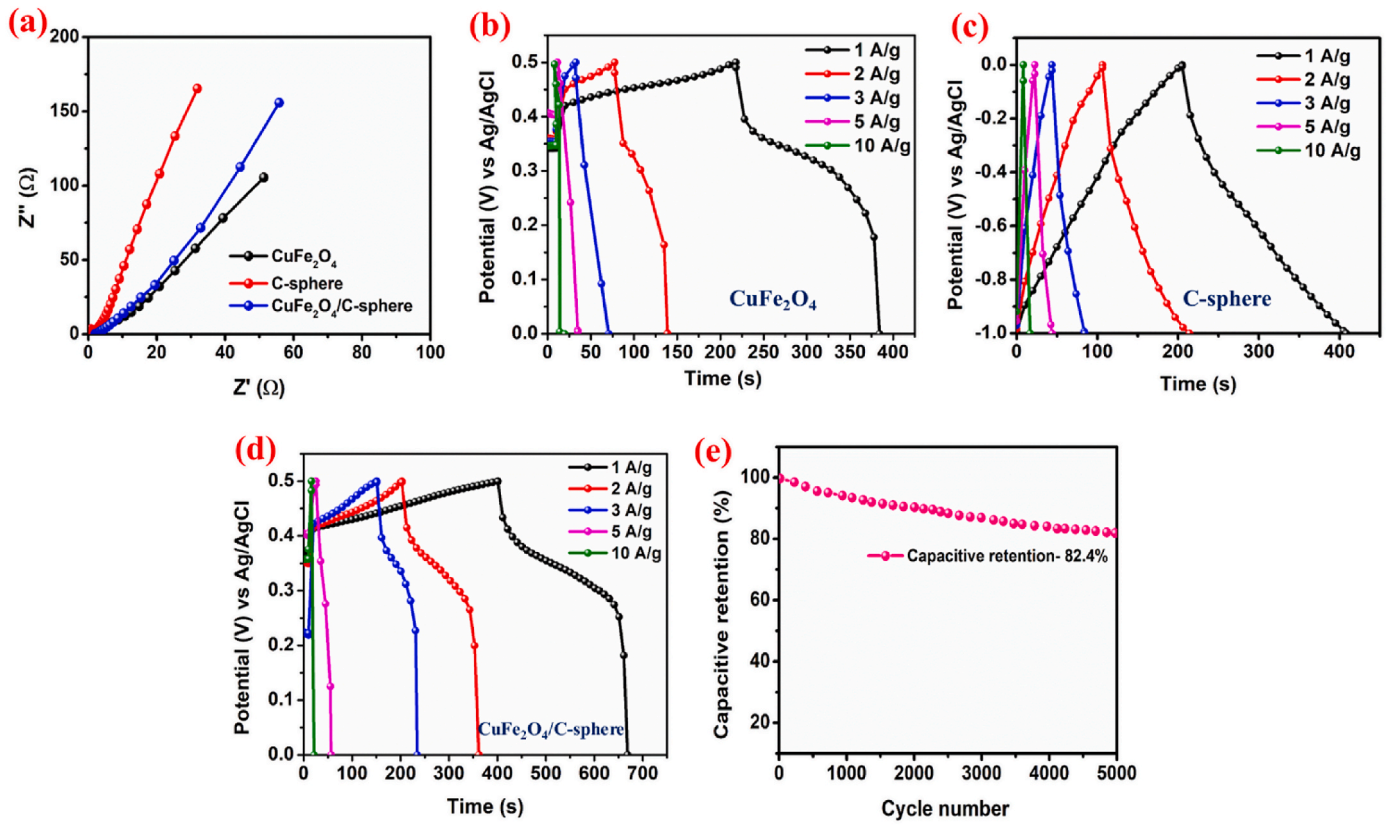


**Fig. 8.** (a) EIS profile at frequency range of 100 kHz- 0.1 Hz, (b–d) GCD profile at different current densities of 1–10 A/g of $CuFe_2O_4$, C-sphere, and $CuFe_2O_4$/C-sphere NC, and (e) cyclic stability at the current density of 10 A/g for 5000 cycles of $CuFe_2O_4$/C-sphere NC.

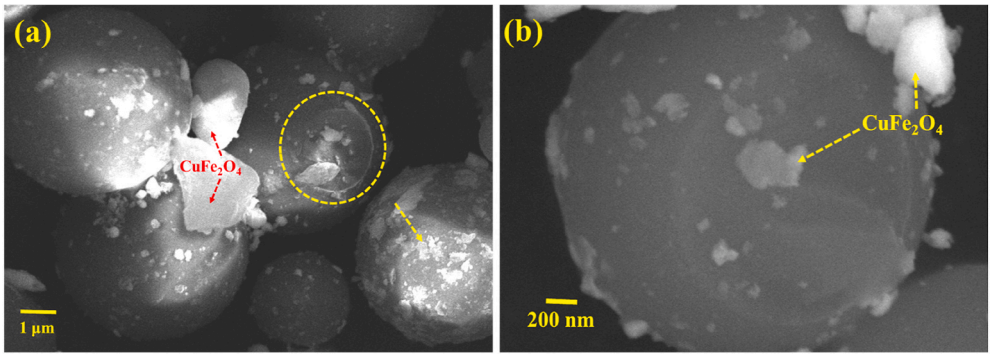


**Fig. 9.** (a,b) SEM image of $CuFe_2O_4$/C-sphere after 5000 cycles.

the increased integral area with an increased scan rate from 10 to 200 mV/s and the redox curves remain analogous even at a high sweep rate of 200 mV/s, signifying their good reversible performance along with their superior rate capability as shown in Fig. 10b.

The internal impedance and diffusion behavior of the $CuFe_2O_4$/C-sphere//AC SHC were studied from the EIS analysis between the frequency range 100 kHz to 0.1 Hz. EIS profile (Fig. 10c) shows the arc-like spectra which deliver the lower solution resistance of 0.85 Ω and the charge transport resistance of about 12.8 Ω, indicating their excellent electrical conductivity and low internal resistance of the device [48].

The charge-discharge characteristics of the $CuFe_2O_4$/C-sphere//AC SHC were investigated by the GCD study. The GCD curves of $CuFe_2O_4$/C-sphere//AC SHC show the typical non-linear performance within the operating potential of 0–1.5 V and also it provides excellent charge-discharge characteristics even at the highest current of 10 A/g, representing their admirable charge storage ability. In addition, the fabricated device demonstrates a low IR drop even at the higher current densities which confirms their exceptional stability and their ability to withstand the higher applied currents as presented in Fig. 10d. The specific capacity of the $CuFe_2O_4$/C-sphere//AC SHC was found to be 131, 128, 96.3, 61, and 46 C/g corresponding current rates of 1, 2, 3, 5, and 10 A/g. Moreover, the cyclic stability tests of $CuFe_2O_4$/C-sphere//AC SHC were analyzed to evaluate the device stability for several charge-discharge cycles [49]. From the cycle test (Fig. 10e), the $CuFe_2O_4$/C-sphere//AC SHC demonstrated excellent stability of 78% even after 3000 charge/discharge cycles.

The energy and power density of the $CuFe_2O_4$/C-sphere//AC SHC determines the actual electrochemical performance compared with the other electrochemical devices. Ragone plot which is a plot between the energy density and power density that shows the electrochemical performance of all devices [50,51]. Ragone plot of $CuFe_2O_4$/C-sphere//AC SHC (Fig. 10f) shows the calculated energy densities were 40.9, 39, 30.5,

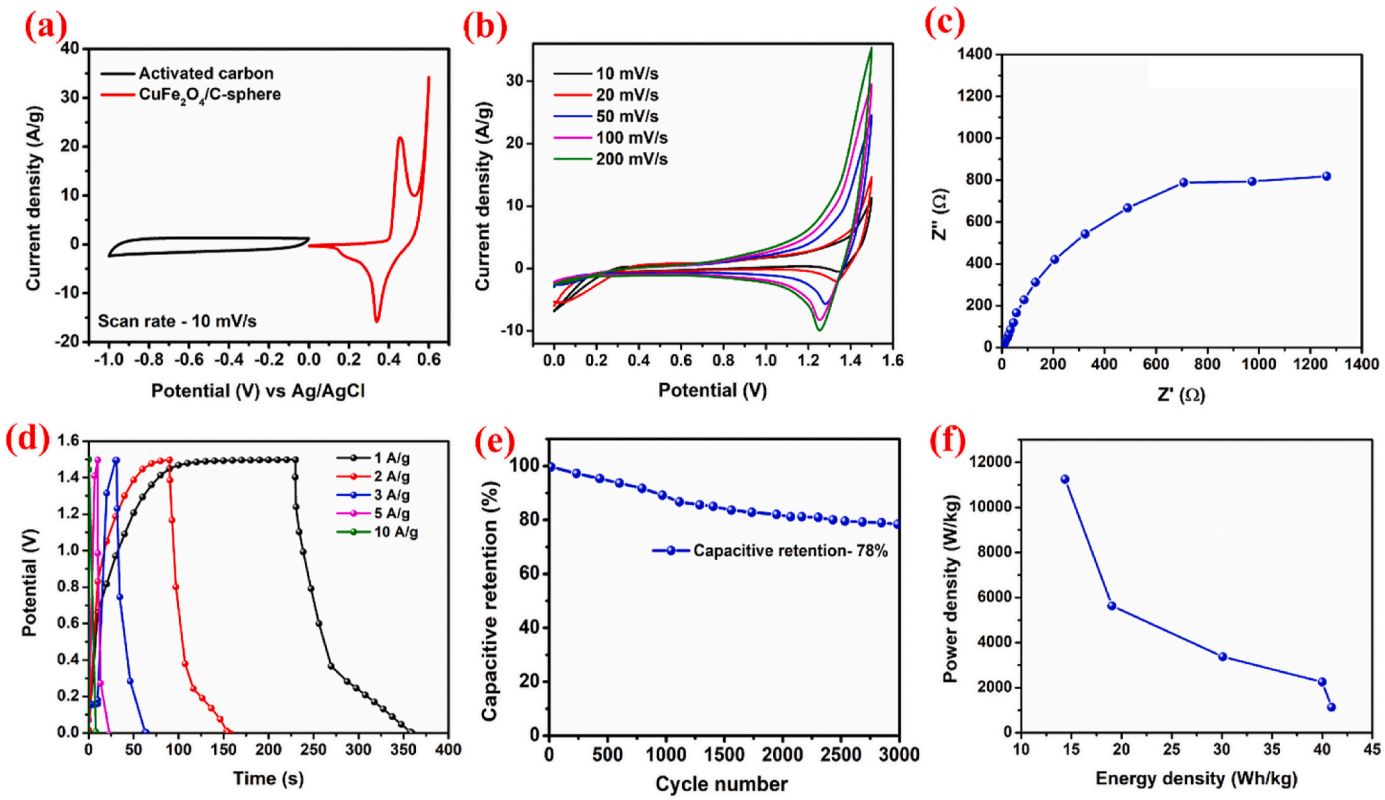


**Fig. 10.** (a) Comparative CV curve of AC and $CuFe_2O_4$/C-sphere at the scan rates of 10 mV/s, (b) CV curve at different scan rates of 10–200 mV/s, (c) EIS profile at frequency range of 100 kHz- 0.1 Hz, (d) GCD profile at different current densities of 1–10 A/g, (e) cyclic stability at the current density of 10 A/g for 3000 cycles, and (f) Ragone plot of $CuFe_2O_4$/C-sphere//AC SHC.

19.6, and 14.4 W h/kg and their actual power densities were calculated as 1123, 2248, 3362, 5612, and 11248 W/kg. It is observed from the Ragone plot, that the energy density (14.4 W h/kg) of the $CuFe_2O_4$/C-sphere//AC SHC even at the higher current density of 10 A/g is higher than the actual supercapacitor energy density which confirms their excellent charge storage performance. The comparison of the electrochemical performance of the $CuFe_2O_4$/C-sphere NC with other reported literature is tabulated in Table 1. From the electrochemical studies, the $CuFe_2O_4$/C-sphere NC demonstrated its own electrochemical potential and it can be used as an alternative for futuristic supercapacitor applications.

## 5. Conclusion

In conclusion, the $CuFe_2O_4$/C-sphere NC was synthesized and successfully applied as an electrode for high energy density solid-state hybrid supercapacitors. HR-TEM confirmed the existence of cubic particles and carbon microsphere particles with a size of 710 nm. CV study confirmed that the competitive specific capacity of $CuFe_2O_4$/C-sphere NC was 320 C/g at 10 mV/s together with long-lasting cyclic stability of 82.4% for 5000 cycles. The fabricated $CuFe_2O_4$/C-sphere//AC SHC delivers a specific capacity of 131 C/g and also it provides an excellent energy density of 40.9 W h/kg and a high power density of 11248 W/kg. This work confirms the $CuFe_2O_4$/C-sphere NC will play a huge role in altering the technologies for the upcoming advanced electronics.

**Table 1**
Comparison of electrochemical activity of $CuFe_2O_4$–C-sphere//AC SHC with reported literatures.

| Material | Specific Capacitance/ Capacity | Energy density (Wh/kg) | Power density (W/kg) | Reference |
|---|---|---|---|---|
| PVA-$CuFe_2O_4$ | 60 C/g at 1 A/g | 18.75 | 3012 | [32] |
| $NiFe_2O_4$ | 140 F/g at 2 A/g | 20.7 | 4000 | [52] |
| $CoFe_2O_4$/C | 160 F/g at 0.25 A/g | 14.38 | 720 | [53] |
| $ZnFe_2O_4$ | 156 F/g at 1 A/g | 5.42 | 4992 | [54] |
| $ZnFe_2O_4$/rGO | 33.6 F/g at 0.5 A/g | 6.7 | 300 | [55] |
| $NiCoFe_2O_4$ | 43 F/g at 5 A/g | 6.4 | 1904.7 | [56] |
| $NiFe_2O_4$/ Graphene | 464.15 F/g at 1 A/g | 14.01 | 70 | [57] |
| $Ni_{0.5}Zn_{0.5}Fe_2O_4$ | 151 F/g at 1 A/g | 17 | 450 | [58] |
| $CuFe_2O_4$/rGO | 360 C/g at 1 A/g | 18.3 | 455 | [59] |
| **$CuFe_2O_4$/C-sphere NC** | **131 C/g** | **40.9** | **11248** | **This Work** |

## CRediT authors statement

†**J J Rushmittha:** Conceptualization, Investigation, Writing-Original Draft, Software. **S. Radhika:** Project administration, Supervision, Writing- Review and Editing. **Khalid A. Alrashidi:** Editing and Fund. **G. Maheshwaran:** Formal analysis, software. **S. Dhinesh:** Data Curation. **S. Sambasivam:** Formal analysis, Review and Editing.

## Declaration of competing interest

The authors declare that they have no known competing financial interests or personal relationships that could have appeared to influence the work reported in this paper.

## Data availability

The data that has been used is confidential.

## Acknowledgment

UAEU strategic research program under grant no. 12R233, and National Water and Energy Centre, United Arab Emirates University, UAE for financial support. The authors are grateful to the Researchers Supporting Project Number (RSPD2024R645) King Saud University, Riyadh, Saudi Arabia.

## Appendix A. Supplementary data

Supplementary data to this article can be found online at https://doi.org/10.1016/j.mtsust.2024.100950.

## References

[1] M. Tawalbeh, H.A. Khan, A. Al-Othman, Insights on the applications of metal oxide nanosheets in energy storage systems, J. Energy Storage 60 (2023) 106656.
[2] D. Mohanty, I.-M. Hung, M. Moniruzzaman, S.K. Satpathy, Unleashing recent electrolyte materials for next-generation supercapacitor applications: a comprehensive review, J. Energy Storage 72 (2023) 108352.
[3] A. Dutta, M. Shirsendu, B. Mitali, B. Tamal, A comprehensive review on batteries and supercapacitors: development and challenges since their inception, Energy Storage 5 (1) (2023) e339.
[4] P. Forouzandeh, V. Kumaravel, S.C. Pillai, Electrode materials for supercapacitors: a review of recent advances, Catalysts 10 (9) (2020) 969.
[5] J. Zhao, J. Zhao, A. Burke, Review on supercapacitors: technologies and performance evaluation, J. Energy Chem. 59 (2021) 276–291.
[6] S. Liu, S. Liu, L. Wei, H. Wang, H. Wang, Review on reliability of supercapacitors in energy storage applications, Appl. Energy 278 (2020) 115436.
[7] X. Zang, C. Shen, M. Sanghadasa, L. Lin, High-voltage supercapacitors based on aqueous electrolytes, Chemelectrochem 6 (4) (2019) 976–988.
[8] J.M. Lim, Y.S. Jang, H.V.T. Nguyen, J.S. Kim, Y. Yoon, B.J. Park, D.H. Seo, K.-K. Lee, Z.J. Han, K. Ostrikov, S.-G. Doo, Advances in high-voltage supercapacitors for energy storage systems: materials and electrolyte tailoring to implementation, Nanoscale Adv. 5 (3) (2023) 615–626.
[9] V.V.N. Obreja, On the performance of supercapacitors with electrodes based on carbon nanotubes and carbon activated material—a review, Physica E: low-dimen Sys, Nanostruc 40 (7) (2008) 2596–2605.
[10] R. Vellacheri, A. Al-Haddad, H. Zhao, W. Wang, C. Wang, Y. Lei, High performance supercapacitor for efficient energy storage under extreme environmental temperatures, Nano Energy 8 (2014) 231–237.
[11] S. Najib, E. Erdem, Current progress achieved in novel materials for supercapacitor electrodes: mini review, Nanoscale Adv. 1 (8) (2019) 2817–2827.
[12] T. Wang, J. Lei, Y.-L. Wang, L.H. Pang, F.-T. Pan, K.-J. Chen, H. Wang, Approaches to enhancing electrical conductivity of pristine metal-organic frameworks for supercapacitor applications, Small 18 (32) (2022) 2203307.
[13] J. Sun, X. Tian, C. Xu, H. Chen, Porous CuCo2O4 microtubes as a promising battery-type electrode material for high-performance hybrid supercapacitor, J. Materiomics 7 (6) (2021) 1358–1368.
[14] H. Sun, Y. Miao, G. Wang, X. Han, Y. Wang, Z. Zhang, C. Luo, X. Liu, C.- yan Xu, H. Chen, Sonochemical synthesis of battery-type ZnCo2O4 electrode material with huge specific surface area for advanced hybrid supercapacitors, J. Energy Storage 76 (2024) 109780.
[15] E. Bao, X. Ren, R. Wu, X.-H. Liu, H. Chen, Y. Li, C.- yan Xu, Porous MgCo2O4 nanoflakes serve as electrode materials for hybrid supercapacitors with excellent performance, J. Colloid Interface Sci. 625 (2022) 925–935.
[16] X. Han, H. Sun, C. yan, Xu, J. Zhu, H. Chen, High-performance asymmetric supercapacitors assembled with novel disc-like MnCo2O4 microstructures as advanced cathode material, J. Colloid Interface Sci. 667 (2024) 350–361.
[17] E. Bao, X. Ren, Y. Wang, Z. Zhang, C. Luo, X.-H. Liu, C.- yan Xu, H. Chen, Advanced hybrid supercapacitors assembled with CoNi LDH nanoflowers and nanosheets as high-performance cathode materials, J. Energy Storage 82 (2024) 110535.
[18] H. Sun, Y. Miao, G. Wang, X. Han, C.- yan Xu, J. Zhu, Battery-type ZnCo2O4 nanosheets and nanowires as advanced cathode materials for hybrid supercapacitors with ultra-long cycling stability, J. Energy Storage 92 (2024) 112189.
[19] M.L. Aparna, A. Nirmala Grace, P. Sathyanarayanan, Niroj Kumar Sahu, A comparative study on the supercapacitive behaviour of solvothermally prepared metal ferrite (MFe2O4, M= Fe, Co, Ni, Mn, Cu, Zn) nanoassemblies, J. Alloys Compd. 745 (2018) 385–395.
[20] J.J. Rushmittha, S. Radhika, G. Maheshwaran, C.M. Padma, Tuning the electrochemical performance of binary CuFe2O4 incorporated by ZnO nanoparticles for high performance hybrid supercapacitors, Inorg. Chem. Comm. 159 (2023) 111728.
[21] A. Khosravi Ghasemi, M. Ghorbani, M. Soleimani Lashkenari, N. Nasiri, Facile synthesize of PANI/GO/CuFe2O4 nanocomposite material with synergistic effect for superb performance supercapacitor, Electrochim. Acta 439 (2023) 141685.
[22] M. Soleimani Lashkenari, A. Khosravi Ghasemi, M. Khalid, S. Shahgaldi, Facile synthesis of N-doped graphene oxide decorated with copper ferrite as an electrode material for supercapacitor with enhanced capacitance, Electrochim. Acta 465 (2023) 142959.
[23] X. Yang, Y. Li, P. Zhang, L. Sun, X. Ren, H. Mi, Hierarchical hollow carbon spheres: novel synthesis strategy, pore structure engineering and application for micro-supercapacitor, Carbon 157 (2020) 70–79.
[24] D. Xiao, Q. Dou, L. Zhang, M. Yalan, S. Shi, S. Lei, H. Yu, X. Yan, Optimization of organic/water hybrid electrolytes for high-rate carbon-based supercapacitor, Adv. Funct. Mater. 29 (42) (2019) 1904136.
[25] Z. Ji, G. Tang, L. Chen, J. Zhong, Y. Chen, G. Zhu, X. Chuan, J. Zhang, X. Shen, Defect engineering of hollow porous N, S co-doped carbon spheres-derived materials for high-performance hybrid supercapacitors, Chem. Eng. J. 480 (2024) 148213.
[26] C. Liu, X. Zhang, Y. Cheng, X. Hao, P. Yang, NiS/Ni3S4 decorated double-layered hollow carbon spheres for efficient electrochemical hydrogen evolution reaction and supercapacitor, Electrochim. Acta 477 (2024) 143751.
[27] M. Israr, J. Iqbal, A. Arshad, A. Sadaf, M. Rani, M. Rani, S. Jabeen, CuFe2O4/GNPs nanocomposites for symmetric supercapacitors and photocatalytic applications, J. Phys. D Appl. Phys. 54 (39) (2021) 395501.
[28] A.K. Ghasemi, M. Ghorbani, M.S. Lashkenari, N. Nasiri, Facile synthesize of PANI/GO/CuFe2O4 nanocomposite material with synergistic effect for superb performance supercapacitor, Electrochim. Acta 439 (2023) 141685.
[29] J.J. Rushmittha, S. Radhika, C.M. Padma, Investigation on ZrO2 supported CuFe2O4 based nanocomposite as a potential electrode for supercapacitors and magnetic applications, Inorg. Chem. Comm 152 (2023) 110720.
[30] S. Vinothini, K. Arjunan, S. Subramanian, C. Te-Wei, V. Naratip, CuFe2O4 nanofiber incorporated with a three-dimensional graphene sheet composite electrode for supercapacitor and electrochemical sensor application, INORGA 12 (6) (2024) 164.
[31] W.H. Lee, J.H. Moon, Monodispersed N-doped carbon nanospheres for supercapacitor application, ACS Appl. Mater. Interfaces 6 (16) (2014) 13968–13976.
[32] J.J. Rushmittha, S. Radhika, G. Maheshwaran, C.M. Padma, Enhanced electrochemical activity of PVA assisted CuFe2O4 nanoparticles as a potential electrode for the fabrication of high energy density hybrid supercapacitor, Inorg. Chem. Comm 157 (2023) 111349.
[33] J. Du, L. Liu, Y. Yu, Y. Zhang, H. Lv, A. Chen, Interpolation strategy for monodisperse hollow mesoporous carbon spheres in high performance supercapacitor, J. Power Sources 434 (2019) 226720.
[34] G. Maheshwaran, P. Pandi, S. Suganya, B. Arjun Kumar, G. Ramalingam, M. Ramesh Prabhu, S. Sudhahar, Fabrication of self charging supercapacitor based on two dimensional bismuthene-graphitic carbon nitride nanocomposite powered by dye sensitized solar cells, J. Energy Storage 56 (2022) 105900.
[35] S.S. Pradeepa, K. Sutharthani, R. Suba Devi, Wei-Ren Liu, M. Sivakumar, Investigation on two-dimensional molybdenum oxide-graphitic carbon nitride (MoO3-g-C3N4) heterostructures based hybrid electrodes for the fabrication of high energy density solid state supercapacitors, J. Taiwan Inst. Chem. Eng. (2023) 105084.
[36] A. Kumar, Sol gel synthesis of zinc oxide nanoparticles and their application as nano-composite electrode material for supercapacitor, J. Mol. Struct. 1220 (2020) 128654.
[37] M. Buldu-Akturk, T. Maryam, T. Ali, E. Emre, ZnO and reduced graphene oxide electrodes for all-in-one supercapacitor devices, Nanoscale 14 (8) (2022) 3269–3278.
[38] Y. He, B. Mingzhu, Y. Heli, Z. Cuijuan, M. Arslan, S. Xiangqian, Y. Shanshan, Nanoscale CuFe2O4 uniformly decorated on nitrogen-doped carbon nanofibers as highly efficient catalysts for polysulfide conversion in lithium-sulfur batteries, Chemelectrochem 8 (23) (2021) 4564–4572.
[39] S. Balamurugan, N. Naresh, I. Prakash, N. Satyanarayana, Ion and Electron-Conducting Additive Effect on Li-Ion Charge Storage Performance of CuFe2O4/SiO2 Composite Aerogel Anode, vol. 46, 2020, pp. 25330–25340.
[40] S. Sundaresan, D. Subramanian, G. Raju, Exploration of two dimensional MoO3-Fe2O3 nanocomposite for the fabrication of high energy density supercapacitor applications, Inorg. Chem. Commun. 148 (2023) 110360.
[41] Y. Shuhua, Z. Han, J. Sun, X. Yang, X. Hu, C. Li, B. Cao, Controllable ZnFe2O4/reduced graphene oxide hybrid for high-performance supercapacitor electrode, Electrochim. Acta 268 (2018) 20–26.
[42] M. Isacfranklin, R. Yuvakkumar, G. Ravi, B. Saravanakumar, M. Pannipara, A. G. Al-Sehemi, D. Velauthapillai, Quaternary $Cu_2FeSnS_4$/PVP/rGO composite for supercapacitor applications, ACS Omega 6 (14) (2021) 9471–9481.
[43] M. Girirajan, N.B. Alagarsamy, K. Ramachandran, R.P. Manimuthu, D. Pazhanivel, K.K. Muthusamy, S. Sakkarapani, Two dimensional layered bismuthene nanosheets with ultra-fast charge transfer kinetics as a superior electrode material for high performance asymmetric supercapacitor, Electrochim. Acta 426 (2022) 140838.
[44] S.S. Pradeepa, K. Sutharthani, R. Subadevi, M. Sivakumar, Exploration, of magnetic sesquioxide nanocomposite as a potential electrode material for the fabrication of high energy density asymmetric supercapacitors, J. Electroanal. Chem. 928 (2023) 117043.
[45] K. Song, R. Yang, X. Wang, B. Zhang, J. Wang, X. Chen, Solvent ratio controlled synthesis of CoFe2O4 hollow skeleton nanobox electrode for high-performance supercapacitor, Appl. Surf. Sci. 533 (2020) 147433.
[46] H. Zhang, H. Zhao, M.A. Khan, W. Zou, J. Xu, L. Zhang, L. Zhang, J. Zhang, Recent progress in advanced electrode materials, separators and electrolytes for lithium batteries, J. Mater. Chem. A 6 (42) (2018) 20564–20620.
[47] M. Safari, J. Mazloom, Electrochemical performance of spindle-like Fe2Co-MOF and derived magnetic yolk-shell CoFe2O4 microspheres for supercapacitor applications, J. Solid State Electrochem. 25 (8–9) (2021) 2189–2200.
[48] Hafeez Ur-Rehman, Shuja Ahmed, Muhammad Ali, M. Shahzad Khan, Imran Murtaza, Hong Meng, Investigation of charge and current dynamics in

PVA–KOH gel electrolyte-based supercapacitor, J. Mater. Sci. Mater. Electron. (2022) 1–14.
[49] H. Zong, J. Dong, Y. He, H. Fu, H. Guo, F. Liu, J. Xu, J. Liu, Flexible asymmetric supercapacitor based on Open-Hollow Nickel-MOFs/Reduced graphene oxide aerogel electrodes, Chem. Eng. J. 475 (2023) 146088.
[50] Qian Zhang, Chaozhe Zhang, Fengjian Yang, Jianhua Yu, Hongzhou Dong, Jing Sui, Yingjie Chen, Liyan Yu, Lifeng Dong, High performance fiber-shaped flexible asymmetric supercapacitor based on MnO2 nanostructure composited with CuO nanowires and carbon nanotubes, Ceram. Int. 48 (10) (2022) 13996–14003.
[51] S. Mishra, P.K. Maurya, A.K. Mishra, 2H–MoS2 nanoflowers based high energy density solid state supercapacitor, Mater, Chem. Phys. 255 (2020) 123551.
[52] V.T. Ajay, G. Aditi Ashok, P. Ingole, High performance flexible supercapacitor based on single precursor derived NiFe2O4 spinel with tailored cationic distribution and oxygen vacancies in acidic medium, Adv. Sustain. Sys (2024) 2400244.
[53] Y. Zhao, X. Yuanguo, Z. Jie, K. Biao, G. Xiwen, L. Dongwei, G. Xiang, et al., Low-crystalline mesoporous CoFe 2 O 4/C composite with oxygen vacancies for high energy density asymmetric supercapacitors, RSC Adv. 7 (87) (2017) 55513–55522.
[54] M. Mandal, N. Alok Kumar, U. Pundrikaksha, Santosini Patra, Subhasri Subudhi, Apurba Mahapatra, Pitamber Mahanandia, Hydrothermal synthesis of ZnFe2O4 anchored graphene and activated carbon as a new hybrid electrode for high-performance symmetric supercapacitor applications, Diamond. Related, Materials 139 (2023) 110300.
[55] Shuhua Yang, Zhenzhen Han, Jing Sun, Xiaopeng Yang, Xun Hu, Cuncheng Li, Bingqiang Cao, Controllable ZnFe2O4/reduced graphene oxide hybrid for high-performance supercapacitor electrode, Electrochim. Acta 268 (2018) 20–26.
[56] M. Mayakkannan, A. Murugan, A. Shameem, V. Siva, S. Sasikumar, S. Thangarasu, S. Asath Bahadur, Investigations on ternary transition metal ferrite: NiCoFe2O4 as potential electrode for supercapacitor prepared by microwave irradiation method, J. Energy Storage 44 (2021) 103257.
[57] X. Gao, B. Jianqiang, W. Weili, L. Haozhe, C. Yafei, H. Xuxia, S. Xiaoning, L. Rui, Morphology-controllable synthesis of NiFe2O4 growing on graphene nanosheets as advanced electrode material for high performance supercapacitors, J. Alloys Compd. 826 (2020) 154088.
[58] B. Nawaz, A. Ghulam, U. Muhammad Obaid, R. Sarish, A. Fazal, Investigation of the electrochemical properties of Ni0.5Zn0.5Fe2O4 as binder-based and binder-free electrodes of supercapacitors, Energies 14 (11) (2021) 3297.
[59] B. Mary, J. Judith Vijaya, Radhika R. Nair, A. Mustafa, P. Stephen Selvamani, B. Saravanakumar, M. Bououdina, L. John Kennedy, Reduced graphene oxide-tailored CuFe2O4 nanoparticles as an electrode material for high-performance supercapacitors, J. Nanomater. 2022 (2022) 9861440.